Durability Evolution and Phase Transformation Mechanisms of Wood-Fiber-Reinforced Magnesium Oxysulfate Composites under Hydrothermal Cycling

Guicheng Xia,[a] Fuqiang He,[a,]* Fajiang Chen,[b] and Yu Fang [a]

*Corresponding author: fqhe@gzu.edu.cn

DOI: 10.15376/biores.21.4.10485-10503

GRAPHICAL ABSTRACT

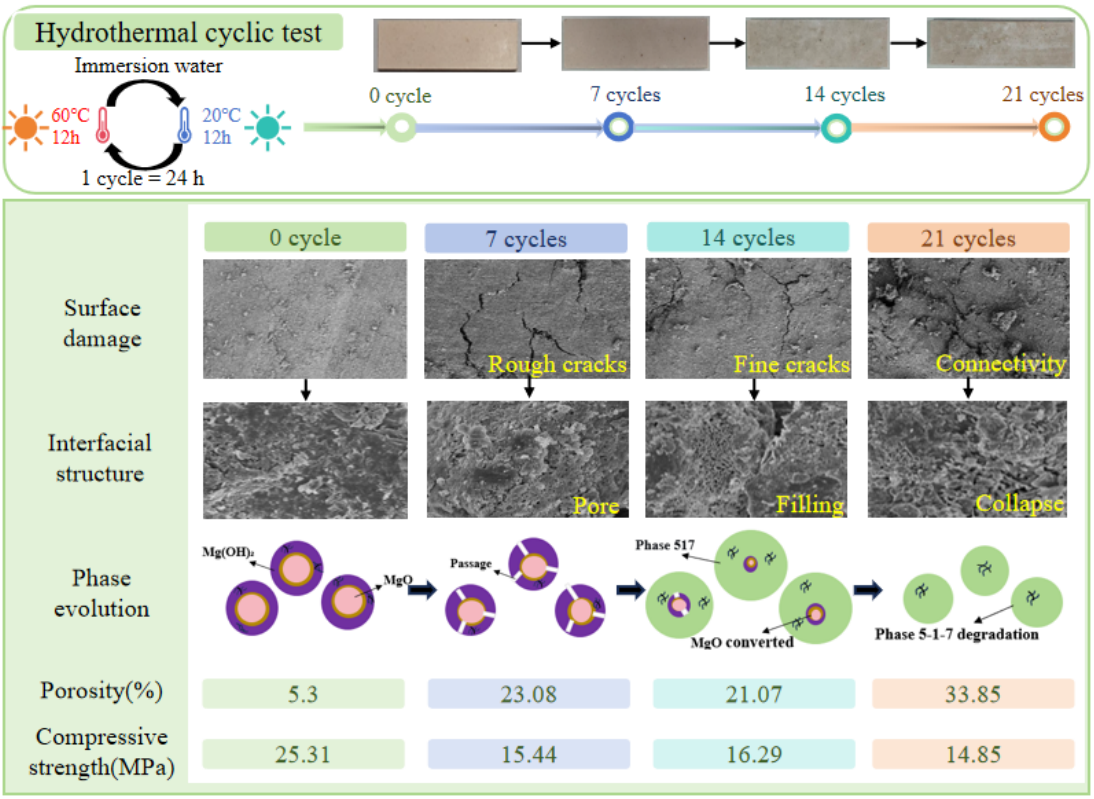

Durability Evolution and Phase Transformation Mechanisms of Wood-Fiber-Reinforced Magnesium Oxysulfate Composites under Hydrothermal Cycling

Guicheng Xia,[a] Fuqiang He,[a,]* Fajiang Chen,[b] and Yu Fang [a]

To evaluate the long-term durability of environmentally friendly biomass composites under hydrothermal conditions, this study investigated the degradation behavior of wood-fiber-reinforced magnesium oxysulfate (MOS) panels subjected to accelerated hydrothermal cycling with alternating immersion at 60 and 20 °C. The results showed non-monotonic changes in mechanical properties and microstructure. After 7 cycles, the diffraction peak associated with the 517-phase ($5Mg(OH)_2{\cdot}MgSO_4{\cdot}7H_2O$) weakened, while residual MgO continued to hydrate. Meanwhile, the porosity increased to 23.1%, and the modulus of rupture (MOR) decreased from 25.3 to 15.4 MPa. At 14 cycles, the porosity decreased slightly to 21.1%, while the MOR increased numerically to 16.3 MPa, indicating a temporary stabilization tendency associated with continued hydration and evolution of MOS hydration products. After 21 cycles, the diffraction features of the 517-phase weakened further, $MgCO_3$-related peaks became more pronounced, and the porosity increased to 33.9%. Interfacial deterioration was also observed, accompanied by a decrease in MOR to 14.8 MPa. Taken together, the hydrothermal durability of the composites was closely associated with the degradation of MOS hydration products, continued hydration of residual reactive components, and pore-structure evolution. These findings provide useful evidence for improving the hydrothermal durability of MOS-based biomass composites.

DOI: 10.15376/biores.21.4.10485-10503

Keywords: Biomass board; Magnesium oxysulfide material; Hydrothermal cycling; Performance evolution

Contact information: a: School of Mechanical Engineering, Guizhou University, Guiyang 550025, China; b: Guizhou Shixiang Technology Co., Ltd, Guiyang 550025, China;
** Corresponding author: fqhe@gzu.edu.cn*

INTRODUCTION

Wood-based composites are pivotal to the global construction sector, with production projected to reach 420 million cubic meters by 2025 (Stark and Cai 2021; Neitzel *et al*. 2022; Ikubanni *et al*. 2024). Among these, high-density panels reinforced with inorganic binders have gained prominence because of their superior hardness and structural integrity (Vitrone *et al*. 2021; Sharma *et al*. 2024). Unlike traditional composites that rely on aldehyde-based resins, these composite materials utilize eco-friendly inorganic adhesives, providing non-combustible and formaldehyde-free properties that align with sustainable building trends (Aiken *et al*. 2021; Petrovic and Thomas 2024).

Among various inorganic binders, magnesium oxysulfate (MOS) cement has shown good potential in biomass composites due to its relatively low alkalinity, rapid hardening behavior, and good compatibility with lignocellulosic fibers. Wood-fiber-reinforced MOS panels usually exhibit good mechanical performance and environmental

advantages. However, their long-term durability under humid and high-temperature conditions remains a major concern, especially in tropical and subtropical regions (Wang *et al*. 2021; Xin *et al*. 2024; Przybek 2025). Under hydrothermal cycling, repeated moisture absorption and temperature changes can accelerate the degradation of the cement matrix and fiber–matrix interface, resulting in strength loss and structural instability. Therefore, understanding the durability evolution of MOS-based biomass composites under hydrothermal conditions is important for their practical application.

Previous studies on MOS cement mainly focused on improving water resistance and stabilizing the hydration products. Some researchers reported that additives such as sepiolite, flue-gas desulfurization (FGD) gypsum, organic phosphates, and silicic acid could regulate the hydration reaction, inhibit $Mg(OH)_2$ formation, and improve the stability of the 517-phase (Li *et al*. 2017; Gu *et al*. 2020; Zhang *et al*. 2024; Hou *et al*. 2026). Accelerated carbonation treatment was also found to densify the fiber–matrix interface and improve short-term performance (Azevedo *et al*. 2024, 2025). Although these studies improved the initial properties of MOS systems, most of them were carried out under static or relatively stable laboratory conditions. The degradation behavior of MOS-based biomass composites under cyclic hydrothermal environments is still not fully understood. In addition, most existing studies have concentrated on material optimization strategies, such as feedstock pretreatment (Song *et al*. 2018; Tupciauskas and Rizhikovs 2020; Yel 2022), binder system ratios (Bekhta *et al*. 2019; Zhang *et al*. 2020), and binder formulations (Theng *et al*. 2019; Sihag *et al*. 2022). Durability assessments have generally been limited to isolated evaluations of mechanical properties (Luthfi *et al*. 2020) and static microstructure observation (Acda 2022; Yan *et al*. 2024). Relatively little attention has been paid to the long-term degradation mechanism under coupled hydrothermal conditions. However, under actual hydrothermal conditions, these factors usually interact with each other. The decomposition and carbonation of the 517-phase can weaken the matrix skeleton, whereas the hygroscopic swelling of wood fibers may accelerate interfacial deterioration. Meanwhile, the continued hydration of residual MgO may promote the secondary formation of hydration products, leading to localized matrix densification. Consequently, degradation and reconstruction processes may coexist and jointly govern the long-term performance evolution of MOS-based biomass composites. However, the coupled evolution of phase composition, pore structure, and interfacial integrity during hydrothermal cycling remains largely unexplored.

Therefore, this study investigated the durability evolution of wood-fiber-reinforced MOS composites under accelerated hydrothermal cycling. The phase composition, pore structure, interfacial morphology, and mechanical properties were analyzed to reveal the relationship between phase evolution and performance degradation during hydrothermal cycling. The results are expected to provide useful evidence for improving the long-term durability of MOS-based biomass composites in humid environments.

EXPERIMENTAL

Raw Materials

The raw materials used in this study included poplar wood fibers, magnesium oxide (MgO), magnesium sulfate ($MgSO_4$), phosphoric acid (H_3PO_4), ammonium dihydrogen phosphate ($NH_4H_2PO_4$), silicon dioxide (SiO_2), and deionized water. The poplar wood fibers were supplied by Guizhou Jingmu Building Materials Co., Ltd. in China, and were

derived from waste generated during solid wood panel processing. These wood waste materials undergo dry crushing, grinding, and screening. The resulting fibers had a diameter of approximately 0.10 to 0.50 mm and a length of approximately 0.20 to 5 mm; approximately 60 wt% of the fibers passed through a 50-mesh screen. MgO was supplied by a manufacturer in Xinjiang, China, and was produced via high-temperature calcination of magnesite. The MgO exhibited an activity index of approximately 63%.

Specimen Preparation

The fabrication process of the biomass composite panels is schematically illustrated in Fig. 1. Initially, the poplar wood fibers were oven-dried to remove residual moisture prior to mixing. Subsequently, the dried wood fibers and MgO were blended at a volume ratio of 9:1 using a mechanical mixer. Before mixing, a magnesium sulfate solution (26 to 30°Bé) containing a compound additive was prepared. The compound additive was prepared by mixing magnesium sulfate solution, ammonium dihydrogen phosphate, phosphoric acid and silicone oil at a mass ratio of 2:1:1:0.02, with a total dosage of 3 wt% relative to the mass of MgO. During stirring, the additive-containing magnesium sulfate mixture was gradually sprayed into the wood fiber-MgO mixture until a homogeneous slurry was obtained. The prepared mixture was then uniformly spread onto a 7075 aluminum alloy plate and subjected to hot pressing using a hydraulic press at 95 °C under a pressure of 12 MPa for 14 min. The hot-pressing process facilitated matrix densification and reduced internal voids within the composite. After demolding, the obtained panels were cured under ambient conditions (23 ± 2°C) for 48 h. Direct sunlight and airflow exposure were avoided during curing to minimize surface cracking. Subsequently, the cured panels were cut into standard specimens using a sawing machine, followed by surface polishing to remove edge burrs.

To ensure experimental consistency, all specimens were prepared from the same batch of panels. Specimens with dimensions of 210 mm × 65 mm × 8 mm were divided into four groups corresponding to 0, 7, 14, and 21 hydrothermal cycles, respectively. Each group contained three replicate specimens, and the reported results were obtained by averaging the values from the three replicate specimens.

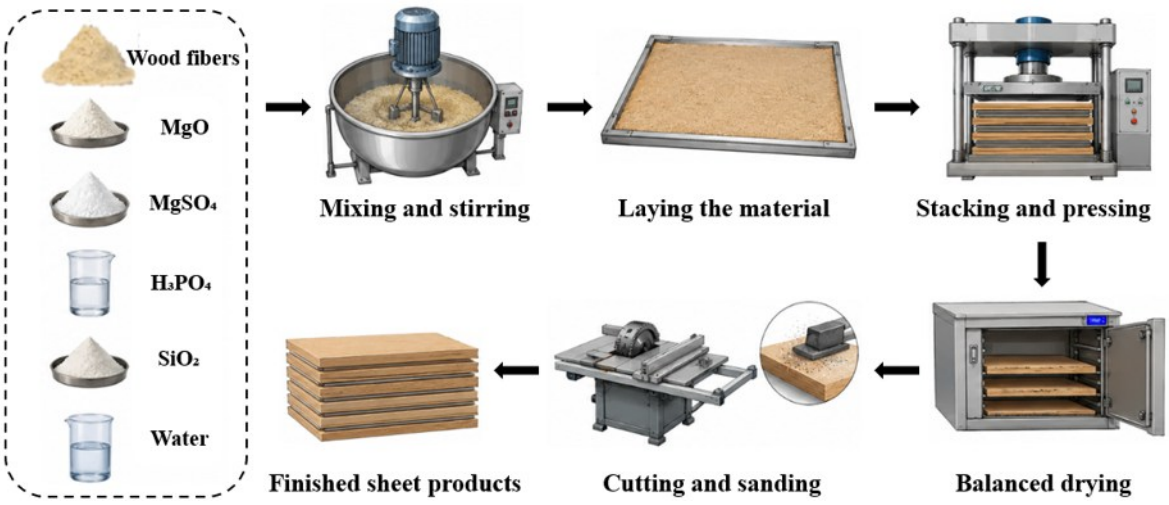

Fig. 1. Preparation process of the plate

Design of Hydrothermal Cycling Test

The hydrothermal cycling test was conducted using an alternating-temperature water immersion method. Initially, the specimens assigned to the 21-cycle group were fully immersed in distilled water at 60 °C for 12 h, followed by immersion in distilled water at 20 °C for an additional 12 h. This procedure constituted one complete 24 h hydrothermal cycle. To ensure simultaneous completion of the cycling treatments, specimens designated for different cycle numbers were introduced into the test at different times. After the first seven cycles, the specimens designated for the 14-cycle group were introduced into the cycling system. Upon completion of 14 cumulative cycles, the specimens belonging to the 7-cycle group were subsequently added. Thereafter, all cycled specimens underwent the remaining cycles under identical test conditions. The selected temperatures (60 °C/20 °C) and exposure durations (12 h for each stage) were not intended to reproduce actual daily temperature fluctuations in a specific region, but were used as an accelerated hydrothermal aging protocol. The 60 °C stage was used to accelerate moisture- and temperature-induced degradation, while the 20 °C stage introduced cyclic temperature variation. Each stage lasted 12 h to allow sustained moisture transport and microstructural evolution. Because the specimens remained fully immersed throughout the test, the imposed conditions were more severe than typical service environments and were therefore used for comparative durability evaluation.

After completing their designated numbers of hydrothermal cycles (7, 14, and 21 cycles), the specimens were removed simultaneously for subsequent physical and mechanical characterization. The 0-cycle specimens served as the unexposed reference group. The reported results represent the average values obtained from three replicate specimens for each group.

Physical Testing

The density of the specimens was determined after hydrothermal cycling, given that density exerts a significant impact on the water resistance and fireproof performance of the biomass panels. Four specimen groups were prepared with consistent initial dimensions and mass, and these parameters were accurately recorded prior to the initiation of the cycling test. Quantitative measurements were performed on each group both before and after the completion of hydrothermal cycling treatments. Specifically, sample dimensions were measured using a vernier caliper with a resolution of 0.05 mm, and mass was measured using a balance with a sensitivity of 0.01 g, calculations were performed according to Eq. 1.

$$\rho = \frac{m}{l \times b \times h} \quad (1)$$

where m is the mass of the test specimen (g), and l, b, and h are the length, width, and thickness of the specimen (mm), respectively.

The expansion ratio of the specimens was assessed following hydrothermal cycling. The thickness swelling (TS) rate was defined as the percentage increment in specimen thickness after exposure to cyclic hydrothermal treatments. Thickness measurements were conducted using a micrometer with a graduation value of 0.01 mm, and the corresponding TS% values were computed in accordance with Eq. 2.

$$TS = \frac{d_2 - d_1}{d_1} \times 100\% \quad (2)$$

where d_1 and d_2 represent the thicknesses (mm) of the biomass polycrystalline wood board samples before and after the experiment, respectively.

The water absorption (WA) rate was evaluated to characterize the water resistance of the specimens. It was defined as the percentage ratio of the moisture mass absorbed by the specimens after hydrothermal cycling to their initial mass before testing, which serves as a critical indicator for evaluating the hydrophilicity, porosity and water resistance of the biomass panels. Its mass was measured using a balance with a sensitivity of 0.01 g. Results were calculated using Eq. 3.

$$WA = \frac{m_2 - m_1}{m_1} \times 100\% \quad (3)$$

where m_1 and m_2 represent the mass of the fiberboard before and after immersion, respectively (g).

Mechanical Testing

The modulus of rupture (MOR) of the biomass polycrystalline panels was tested in accordance with GB/T 17657-2022 using a three-point bending method (Zhang *et al*. 2025). A universal testing machine specifically designed for wood-based panels (BOS-10KNW, Xiamen Boshi Testing Equipment Co., Ltd.) was used for the test. The span length between the two supports was set at 160 mm, and the crosshead speed was controlled at 10 mm/min. During the bending test, the load was applied steadily until the specimen fractured, and the corresponding maximum load was recorded in real time. The MOR values were subsequently calculated in accordance with Eq. 4.

$$MOR = \frac{3FL}{2bh^2} \quad (4)$$

where *M is* the maximum load (N), *L* is the span length (mm), *b* is the specimen width (mm), and *h* is the specimen thickness (mm).

Microstructural Characterization

X-ray diffraction (XRD) was used to examine phase changes in samples at different cycle counts and to investigate the effects of the degree of hydration and crystal structure on the mechanical properties of the panels. Biomass composite board specimens were analyzed using a benchtop X-ray diffractometer (Bruker-D8 ADVANCE, Germany). The XRD instrument employed a copper target, operating at 40 kV, with a 2θ range of 10° to 80°, a current of 40 mA, and a scanning speed of 10°/min.

Scanning electron microscopy (SEM) was used to examine the microstructure and elemental distribution of the cross-section of the panel, and to evaluate the interfacial bond strength and damage at the fiber-matrix interface. A scanning electron microscope (Zeiss Sigma 360, Germany) was used to observe the microstructure of sample surfaces after different numbers of cycles.

The Brunauer-Emmett-Teller (BET) method was employed to monitor changes in surface porosity. After mechanical testing, representative specimens from each hydrothermal-cycle group were pre-dried in a thermostatic oven at 45 °C for 36 h to reduce residual moisture. All groups were subjected to the same pre-drying procedure. Before nitrogen adsorption measurements, the samples were degassed at 120 °C for 8 h in a physical adsorption analyzer (Quantachrome Nova E, USA). Nitrogen adsorption – desorption measurements were then performed at 77.3 K to determine the specific surface area and pore-size distribution.

Statistical Analysis

All physical and mechanical data are presented as mean ± SD of three replicate specimens (n = 3). The experimental data were analyzed and plotted using Origin software. Analysis of variance (ANOVA) was used to assess statistical significance among the different hydrothermal cycling groups, followed by Tukey's multiple comparison test.

RESULTS AND DISCUSSION

Evolution of Physical Properties

Figure 2(a) illustrates the density variation of the panels over the course of hydrothermal cycling. The density decreased from an initial value of 1.89 g/cm³ to 1.86 g/cm³ after 7 cycles, then slightly increased to 1.87 g/cm³ after 14 cycles, before decreasing to 1.82 g/cm³ after 21 cycles. No significant differences were observed among the 0, 7, and 14-cycle groups ($p > 0.05$), whereas the density after 21 cycles was significantly lower than that of the other groups ($p < 0.05$). These numerical variations suggest progressive microstructural evolution within the composite matrix as hydrothermal cycling progressed. The initial slight decrease in density may be associated with partial degradation of the 517-phase and the accompanying development of internal pores. The small numerical increase observed at 14 cycles may be related to continued hydration of residual reactive components and the associated evolution of MOS hydration products, consistent with the subsequent XRD observations. However, this change was not statistically significant, indicating that any temporary densification was limited. Upon further cycling to 21 cycles, prolonged hydrothermal exposure promoted further degradation of the hydration products and development of the pore structure, resulting in a significant decrease in panel density.

Figures 2(b) and 2(c) show the evolution of thickness swelling and water absorption during hydrothermal cycling. The thickness swelling increased from 3.32% at 0 cycles to 3.51%, 6.41%, and 12.0% after 7, 14, and 21 cycles, respectively. No significant difference was observed between the 0-cycle and 7-cycle groups ($p > 0.05$), whereas significant increases occurred after 14 and 21 cycles ($p < 0.05$). In contrast, the water absorption increased significantly from 3.37% to 4.24%, 8.57%, and 13.7% with increasing cycle number ($p < 0.05$).

The different early-stage responses of these two parameters indicate that water uptake preceded pronounced dimensional swelling. During the initial cycling stage, the matrix retained sufficient integrity to partially restrict the moisture-induced expansion of the wood fibers, although water penetration had already increased. With further cycling, degradation of the MOS hydration products and the development of pores and interconnected transport pathways facilitated greater water penetration into the composite. Increased exposure of the wood fibers to moisture subsequently intensified their swelling, resulting in the marked increases in both water absorption and thickness swelling observed after 14 and 21 cycles.

Mechanical Property Response

Figure 2(d) shows the variation in modulus of rupture (MOR) of the panels after different numbers of hydrothermal cycles. After 7 cycles, the MOR decreased markedly from the initial value of 25.3 to 15.4 MPa. A slight numerical increase to 16.3 MPa was observed after 14 cycles; however, this increase was not statistically significant compared with the 7-cycle group ($p > 0.05$). After 21 cycles, the MOR decreased again to 14.8 MPa.

The non-monotonic variation in MOR may be associated with the progressive evolution of the internal microstructure during hydrothermal cycling. Possible contributing factors include continued hydration of residual MgO, changes in the stability of the 517-phase, and the accompanying evolution of the pore structure and the fiber–matrix interface. In particular, the slight numerical increase observed after 14 cycles may reflect a temporary stabilization of the microstructure rather than a significant recovery in mechanical performance. The following microstructural analyses therefore focus on changes in phase composition, pore structure, and interfacial morphology at different cycle counts to further clarify the mechanisms underlying the evolution of MOR.

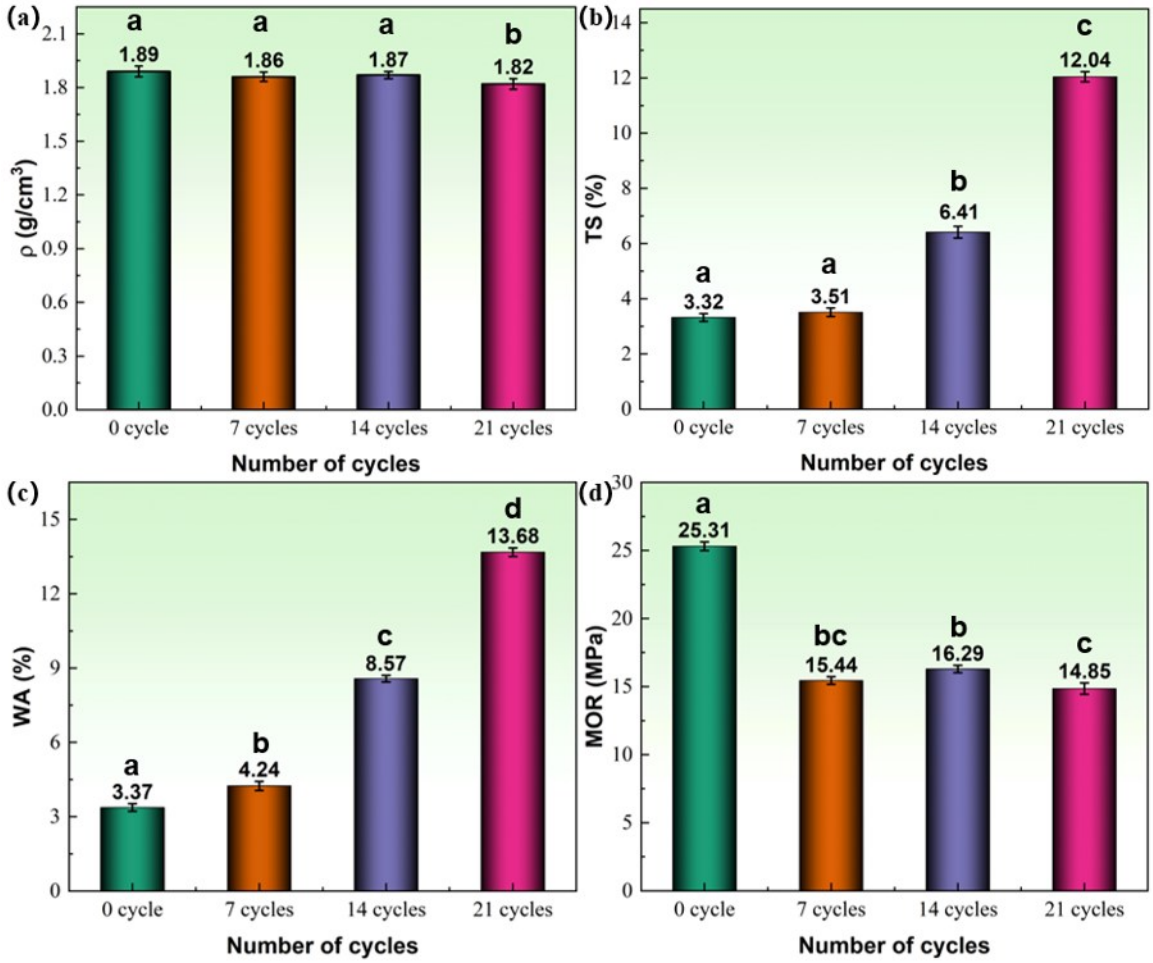

Fig. 2. Changes in physical and mechanical properties at different hydrothermal cycle counts: (a) density; (b) thickness swelling; (c) water absorption; and (d) modulus of rupture. Data are presented as mean ± SD (n = 3). Different lowercase letters indicate significant differences among groups according to one-way ANOVA followed by Tukey's post hoc test ($p < 0.05$).

Phase Composition Analysis

Figure 3 presents the evolution of crystalline phases in the panels subjected to different hydrothermal cycling conditions. After 7 cycles, the diffraction peaks associated with residual MgO weakened markedly, while those associated with $Mg(OH)_2$ became more pronounced, indicating that the residual MgO continued to hydrate during hydrothermal exposure. The diffraction features associated with silica-related phases weakened, which may be related to interfacial reactions between silica species and

hydroxyl groups on the wood fiber surface. Such interactions could enhance interfacial compatibility between the inorganic matrix and wood fibers, thereby partially alleviating the early-stage strength degradation (Ding *et al*. 2022; Liu *et al*. 2022). At the same time, the characteristic diffraction peak of 517-phase weakened, indicating that the primary hydrated magnesium sulfate product had undergone partial degradation. This phase evolution was consistent with the significant decrease in MOR observed during the early stages of the hydrothermal cycling.

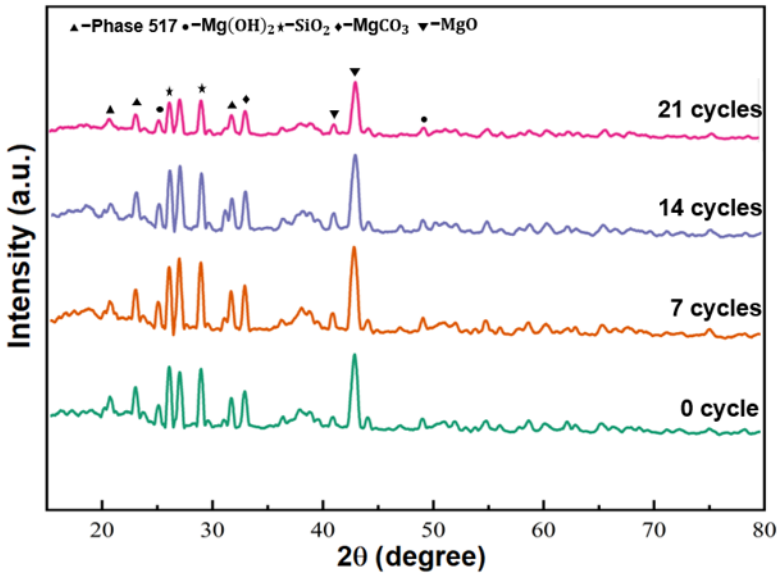

Fig. 3. X-ray diffraction patterns

After 14 cycles, the MgO-related diffraction peaks weakened further, indicating continued consumption of residual reactive MgO. The diffraction features associated with the 517-phase showed a slight increase relative to those after 7 cycles. However, because the present XRD analysis was based on relative diffraction-peak changes rather than quantitative Rietveld refinement, this variation cannot be regarded as definitive evidence for the reformation of the 517-phase. The slight numerical increase in MOR observed after 14 cycles was also not statistically significant. Therefore, this stage is more appropriately interpreted as a tendency toward temporary stabilization, which may be associated with continued hydration of residual reactive components and further evolution of MOS hydration products.

After 21 cycles, the $MgCO_3$-related diffraction peaks became more pronounced, accompanied by a marked weakening of the diffraction features associated with the 517-phase. This phenomenon suggests that prolonged hydrothermal cycling promoted further degradation of magnesium oxysulfate (MOS) hydration products, generating $Mg(OH)_2$ and soluble sulfate species. The formation of the carbonate-containing phases may be related to a reaction with inorganic carbon dissolved in the immersion water, or to reactions triggered by exposure to atmospheric carbon dioxide during sample preparation and pretreatment prior to characterization. Because the present experiments cannot distinguish the relative contributions of these pathways, the exact stage at which carbonation occurred remains uncertain. The progressive decomposition of the 517-phase and the accumulation of carbonation products weakened the integrity of the inorganic matrix and increased internal porosity, ultimately leading to substantial deterioration of the panel strength (Dong

et al. 2025). Overall, the continuous degradation of the MOS hydration products, along with the resulting changes in pore structure and matrix integrity, is consistent with the further decline in MOR observed after prolonged hydrothermal cycling.

Surface Morphology Observation

Figure 4 presents the macroscopic morphological evolution of the specimens subjected to different numbers of hydrothermal cycles. The untreated specimen shown in Fig. 4(a) exhibits a relatively dense and intact structure with smooth surfaces and well-preserved edge morphology. In contrast, the cross-sectional morphologies after hydrothermal cycling, shown in Fig. 4(b), reveal progressively greater structural deterioration with increasing cycle number.

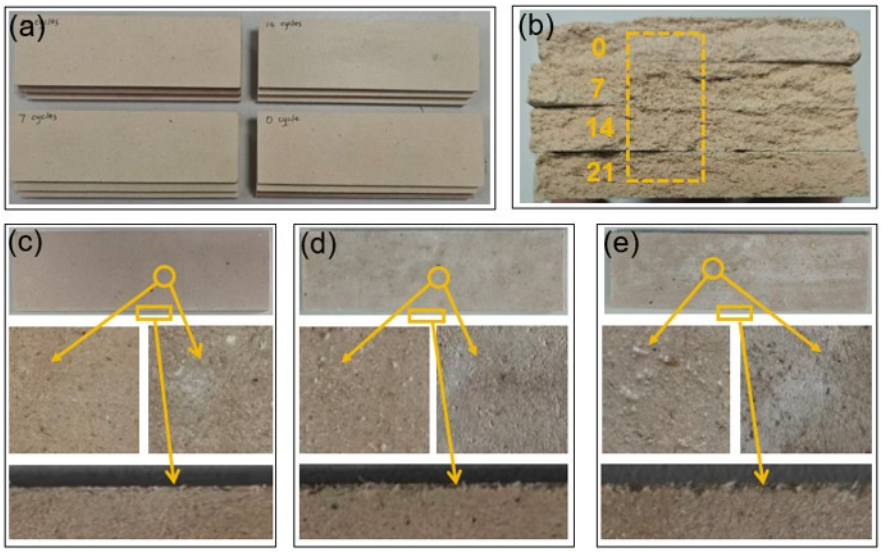

Fig. 4. Cross-sectional views: (a) Specimen before treatment; (b) Cross-sectional morphology after treatment; (c) Cross-section of the 7-cycle group; (d) Cross-section of the 14-cycle group; and (e) Cross-section of the 21-cycle group

The 0-cycle specimen displayed a dense cross-sectional morphology with well-preserved matrix integrity. After 7 cycles, localized microcracks were visible near the edges of the cross-section. At 14 cycles, these cracks extended further toward the center of the cross-section. By 21 cycles, the cracks became wider and more pronounced, accompanied by discoloration and visible structural deterioration. Figure 4(c) presents the surface morphology of the 7-cycle specimen. The surface remains relatively smooth and dense, with clear and regular edge contours. Only a small number of white crystalline deposits are sparsely distributed on the surface, suggesting that the overall structure remains relatively intact at this stage and that moisture absorption and expansion effects are not yet significant. As the cycle number increases to 14 cycles (Fig. 4d), noticeable deformation has appeared along the edges of the panels, with localized areas of the surface becoming raised and rough. The amount of white crystalline deposits also increases slightly, indicating progressive deterioration of the surface structure during repeated hydrothermal treatment. By the 21st cycle (Fig. 4e), white crystalline deposits become more abundant and cover a larger portion of the specimen surface. Severe edge deformation and fiber separation are observed. Simultaneously, surface wood fibers exhibit pronounced

loosening and bulging, accompanied by local fiber disintegration, resulting in a substantial decline in the overall structural integrity of the specimen.

The macroscopic morphological evolution is consistent with the observed changes in physical and mechanical properties. During the early cycling stage, the specimens retained relatively good structural integrity, consistent with the relatively low water absorption and thickness swelling observed at this stage. However, prolonged hydrothermal exposure progressively weakened the matrix structure and increased defect development, thereby facilitating water penetration and accelerating the deterioration of dimensional stability and mechanical performance.

Processing of the SEM images shown in Fig. 5 yielded the pore distribution maps presented in Fig. 6, from which the pore parameters summarized in Table 1 were obtained. The quantified pore features revealed a general increase in pore development with increasing hydrothermal cycles. The detected pore count increased from 763 in the untreated specimen to 1390 after 21 cycles. Meanwhile, both the average pore size and porosity exhibited non-monotonic variation trends. The average pore size increased from 4.59 μm to 15.7 μm, while the porosity increased from 5.3% to 33.9%.

Specifically, the porosity increased markedly from 5.3% to 23.1% after 7 cycles, followed by a slight decrease to 21.1% after 14 cycles, before reaching a maximum value of 33.9% after 21 cycles. The temporary reduction in porosity observed at the intermediate stage suggests that continued hydration of residual reactive components and the associated evolution of MOS hydration products may have partially offset pore development. This trend corresponds to the slight numerical increase in MOR after 14 cycles.

Figure 7 presents representative SEM micrographs and corresponding pore distribution maps illustrating the interfacial evolution of the specimens during hydrothermal cycling. In the processed pore maps, red, yellow, and green regions represent relatively large, medium-sized, and small pores, respectively, while the remaining dark regions correspond to dense matrix areas. The results indicate that both pore size and pore connectivity increased significantly with increasing cycle number. At 0 cycles, the pore structure remained relatively compact, with only limited large pores observed. After prolonged hydrothermal cycling, pore coalescence and crack propagation became increasingly pronounced. By 21 cycles, many medium-sized and small pores had interconnected to form larger void regions, resulting in severe interfacial deterioration and matrix fragmentation.

Combined with the phase evolution results, these observations suggest that prolonged hydrothermal exposure progressively destabilized the MOS hydration products. During the intermediate cycling stage, residual reactive MgO may have continued to hydrate, and the associated evolution of hydration products may have partially compensated for pore development. However, after extensive cycling, the reduced amount of residual reactive MgO may have limited further evolution of MOS hydration products capable of partially compensating for internal damage. At the same time, the more pronounced carbonate-related diffraction features observed after 21 cycles suggest that carbonation-related reactions may also have occurred. These reactions may have involved inorganic carbon dissolved in the immersion water and/or atmospheric CO_2 during subsequent sample handling and preparation. Overall, the continued degradation of MOS hydration products, together with pore enlargement and interfacial deterioration, is consistent with the reductions in density and MOR observed after prolonged hydrothermal cycling.

Table 1. Statistical Analysis of Image Porosity

Samples	Pore	Average Pore Size (μm)	Porosity (%)
0 cycle	763	4.59	5.3
7 cycles	1163	9.34	23.08
14 cycles	1221	9.21	21.07
21 cycles	1389	15.69	33.85

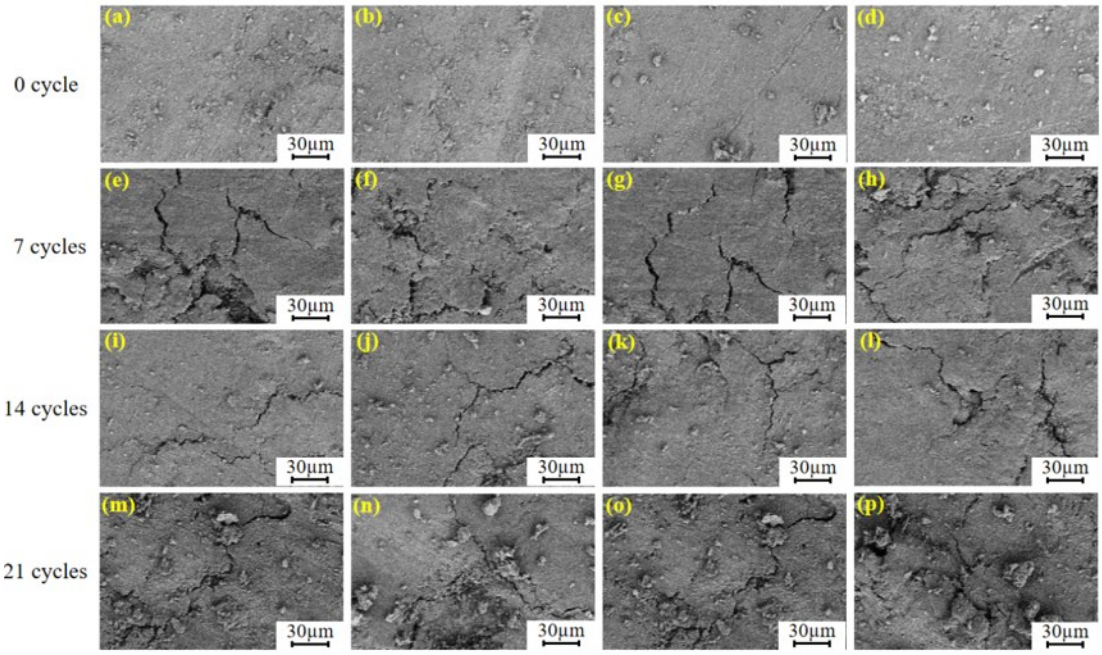

Fig. 5. Original SEM image of the interface

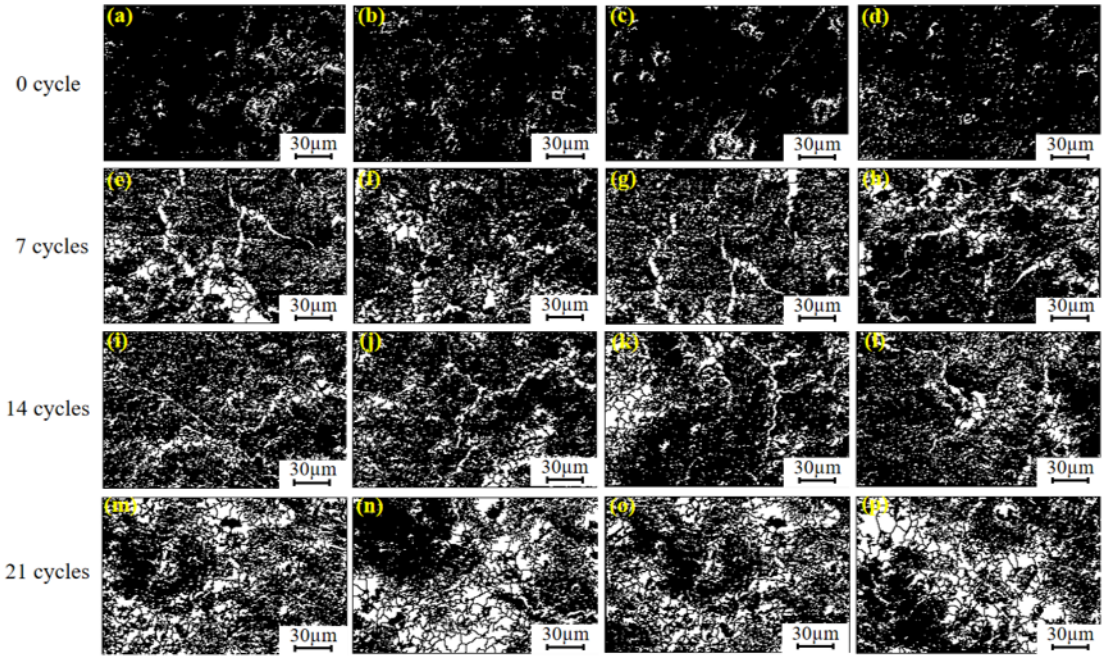

Fig. 6. Pore distribution of the processed image

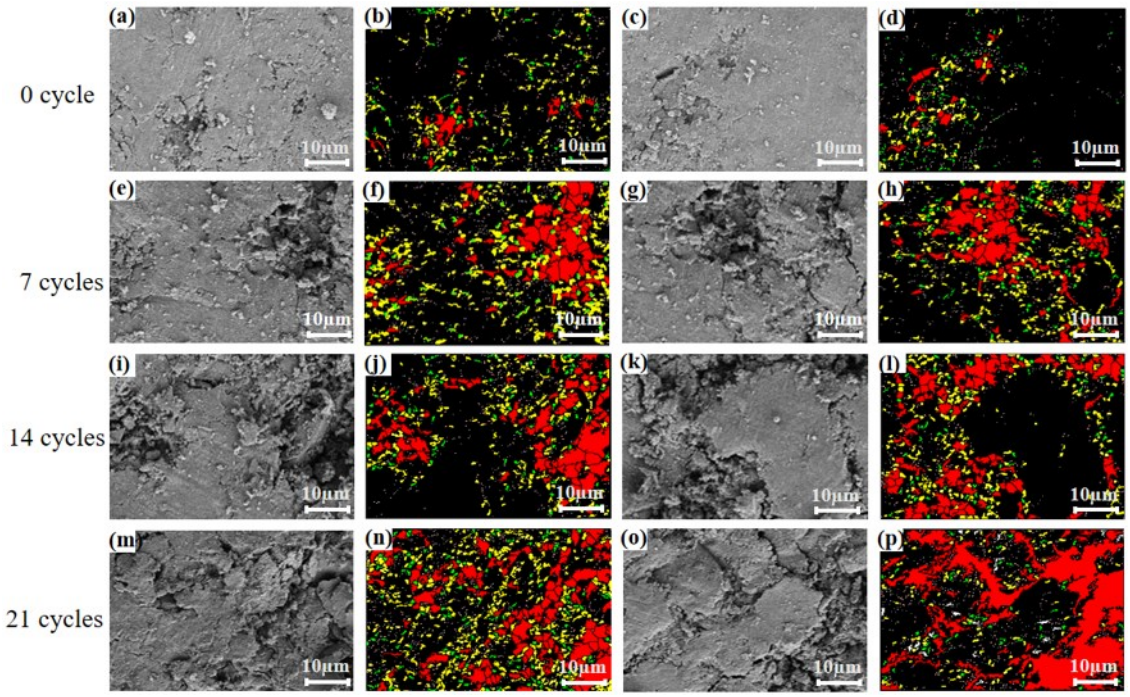

Fig. 7. Evolution of pore structure in samples during hydrothermal cycling: (a, c, e, g, i, k, m, o) SEM images, (b, d, f, h, j, l, n, p) corresponding pore distribution maps

Pore Structure Characterization

Figure 8 presents the nitrogen adsorption–desorption isotherms and corresponding BJH pore size distribution curves of the specimens subjected to different hydrothermal cycles. All samples exhibited typical Type-IV isotherms with distinct hysteresis loops, indicating the presence of mesoporous structures within the composite (Zhang *et al*. 2026). The adsorption capacity gradually increased with increasing relative pressure, while a pronounced separation between the adsorption and desorption branches was observed in the high-pressure region, suggesting the existence of interconnected pore structures (Calzaferri *et al*. 2023). Among all groups, the untreated specimen exhibited the lowest adsorption capacity and smallest pore volume, indicating a relatively compact internal structure. After hydrothermal cycling, the adsorption capacity increased progressively, reflecting the development of additional pores and internal defects. The 21-cycle specimen showed the highest adsorption capacity and broadest pore distribution, indicating severe structural deterioration after prolonged hydrothermal exposure.

The BJH pore size distribution curves further revealed the evolution of the pore structure during cycling. The untreated specimen displayed a relatively concentrated pore size distribution, primarily within the range of 2 to 10 nm, indicating a comparatively uniform pore structure. After 7 cycles, the pore size distribution broadened considerably, and a secondary peak appeared near 30 nm, suggesting the formation of larger mesopores. After 14 cycles, the pore distribution became relatively more uniform, which may be associated with continued hydration of residual reactive components and the associated evolution of MOS hydration products. However, after 21 cycles, the pore distribution became highly dispersed, accompanied by the appearance of multiple characteristic peaks, indicating severe pore coalescence and structural degradation.

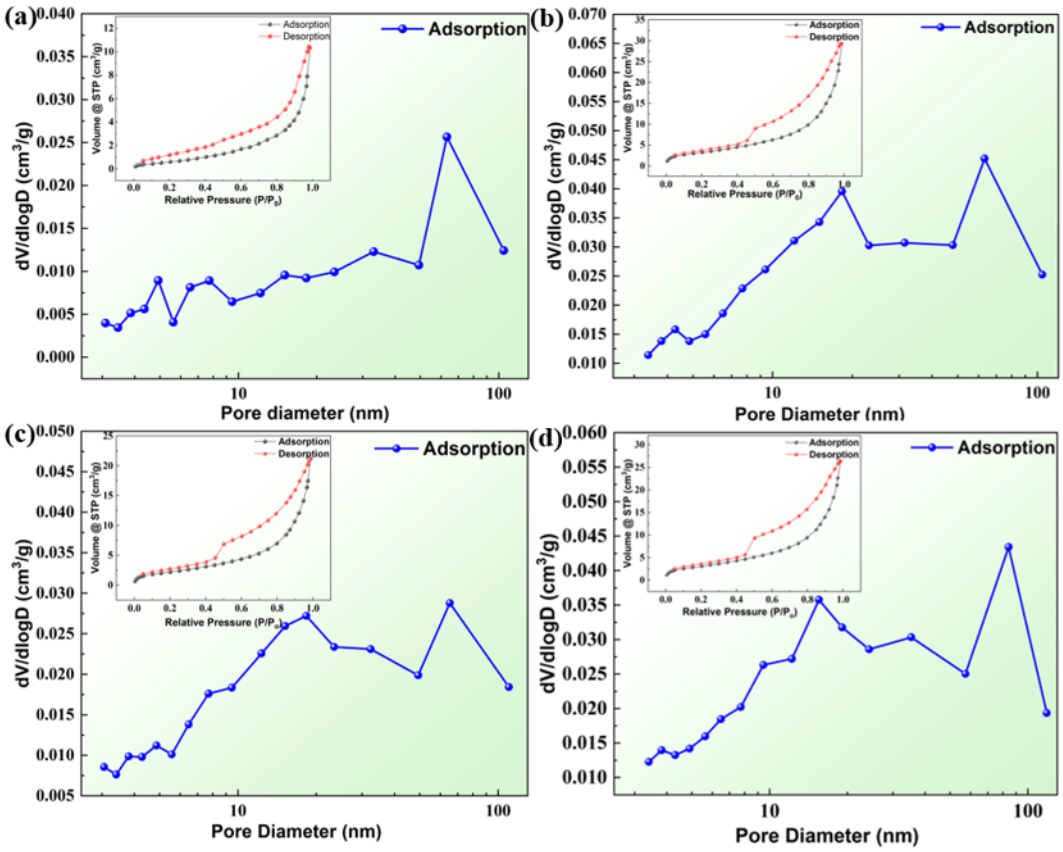

Fig. 8. N_2 adsorption–desorption isotherms and pore size distributions of samples under different hydrothermal cycling times: (a) 0 cycle; (b) 7 cycles; (c) 14 cycles; (d) 21 cycles

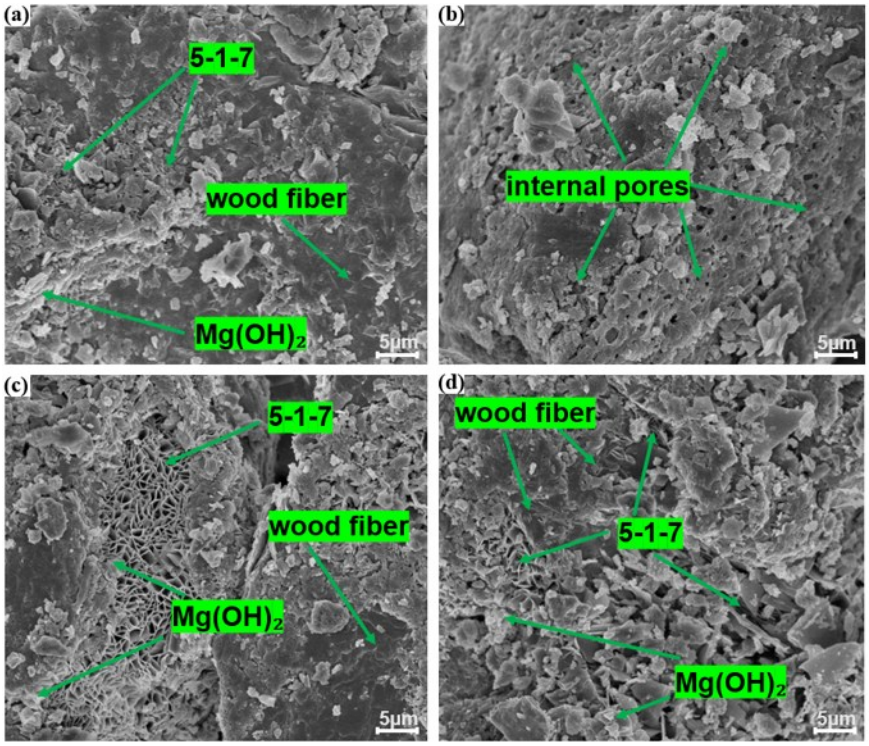

Fig. 9. SEM images of fracture surfaces: (a) 0 cycle; (b) 7 cycles; (c) 14 cycles; (d) 21 cycles

After processing the fracture surface shown in Fig. 4(b), the images presented in Fig. 9 were obtained. The analysis indicated that after 7 hydrothermal cycles, degradation of MOS hydration products was accompanied by pronounced pore development. Although mesopores remained dominant, a large number of pores around 30 nm appeared in the matrix (Fig. 9b). Compared with the 7-cycle group, the 14-cycle group exhibited a more uniform pore size distribution. This change may be associated with continued hydration of residual reactive MgO and further evolution of MOS hydration products, the newly formed 517-phase filled part of the pores, causing the characteristic peak near 30 nm to disappear and forming fine pores of approximately 16 nm at the interface, demonstrating the pore-filling effect of the 517-phase (Fig. 9c). After 21 cycles, the pore structure became increasingly disordered, consistent with continued degradation of MOS hydration products and progressive pore interconnection. The reduced amount of residual reactive MgO may also have limited the ability of continued hydration to compensate for further pore development, ultimately resulting in a disordered pore structure and an increase in porosity (Fig. 9d).

Mechanism of Performance Evolution

Based on the results of mechanical testing, XRD analysis, SEM observations, and pore structure characterization, the performance evolution of the wood-fiber-reinforced MOS composites during hydrothermal cycling can be divided into three distinct stages: initial degradation (0 to 7 cycles), temporary stabilization (7 to 14 cycles), and further deterioration (14 to 21 cycles), as illustrated in Figs. 10 and 11.

After 7 hydrothermal cycles, the diffraction features associated with the 517-phase decreased noticeably, while the $Mg(OH)_2$-related peaks became more pronounced. These changes suggest partial degradation of the 517-phase and are consistent with continued hydration of residual reactive MgO under hydrothermal conditions. At the same time, the porosity increased from 5.30% to 23.1%, accompanied by a decrease in MOR from 25.3 to 15.4 MPa. SEM observations also revealed the appearance of microcracks and enlarged pores. These results suggest that degradation of MOS hydration products was associated with weakening of the matrix structure and progressive development of internal defects.

After 14 cycles, the porosity decreased slightly to 21.1%, while the MOR increased slightly to 16.3 MPa. However, compared with the 7-cycle group, this difference was not statistically significant. XRD analysis indicated that, compared with the 7-cycle group, the diffraction features associated with the 517-phase showed a slight increase. This may be related to the continued hydration of residual active MgO and the further evolution of MOS hydration products, which may have partially offset pore development and structural degradation at this stage.

With further cycling to 21 cycles, the diffraction features associated with the 517-phase decreased again, while $MgCO_3$-related peaks became more pronounced. Meanwhile, porosity reached 33.9%, and extensive crack development was observed in the SEM images. At this stage, the reduced amount of residual reactive MgO may have limited the ability of continued hydration to compensate for further structural deterioration. In addition, continued degradation of the 517-phase, together with the evolution of carbonate-containing phases and the pore structure, may have contributed to further deterioration of the matrix and fiber-matrix interface. As a result, the density and MOR decreased further.

Overall, the performance evolution of the composites during hydrothermal cycling was controlled by two opposite processes. On the one hand, decomposition of the 517-phase increased pore development and reduced structural integrity. On the other hand,

hydration of residual MgO promoted the formation of new hydration products, which partially compensated for the damage during the intermediate stage. As hydrothermal cycling continued, the compensating effect gradually disappeared, and degradation became the dominant process, resulting in the final deterioration of the composites.

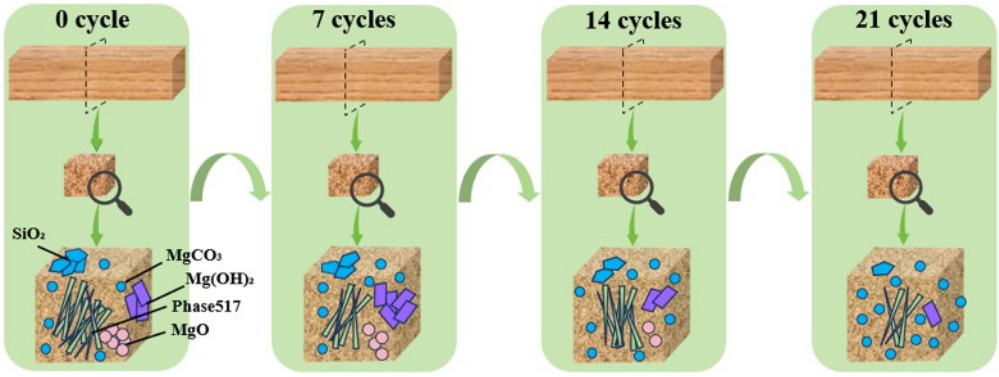

Fig. 10. Phase changes

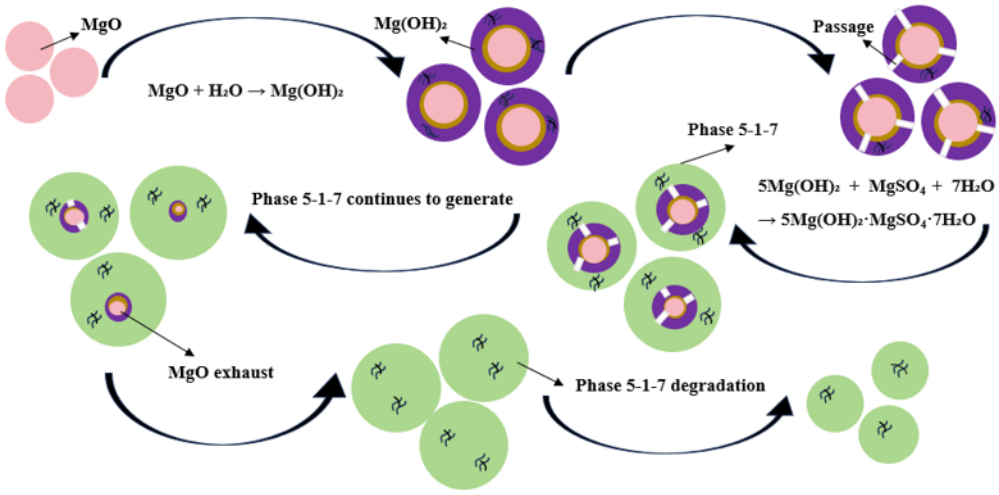

Fig. 11. Reaction mechanism

Collectively, the results demonstrate that the hydrothermal durability of the panels is closely associated with the stability and evolution behavior of 517-phase. Future studies should focus on improving the stability of magnesium oxysulfate hydration products and enhancing interfacial compatibility within the composite system to further improve the long-term durability of the panels under humid and high-temperature environments.

CONCLUSIONS

This study investigated the durability evolution of wood-fiber-reinforced magnesium oxysulfate composites under accelerated hydrothermal cycling through mechanical testing, phase analysis, microstructural observation, and pore structure characterization. The main conclusions are as follows:

1. Hydrothermal cycling significantly affected the physical and mechanical properties of the composites. The density decreased from 1.89 to 1.82 g/cm³, while the water

absorption and thickness swelling increased to 13.7% and 12.0%, respectively. The MOR showed a non-monotonic evolution trend, decreasing from 25.3 to 15.4 MPa after 7 cycles, followed by a slight numerical rise to 16.3 MPa at 14 cycles. However, this was only temporary stabilization, and the strength finally declined to 14.8 MPa after 21 cycles.

2. The evolution of MOS hydration products was closely associated with the durability behavior of the composites. Partial decomposition of the 517-phase during the early stage increased pore development and reduced matrix integrity. During the intermediate stage, the ongoing hydration of residual MgO and the resulting MOS hydration products may have partially offset the ongoing degradation process, leading to a slight decrease in porosity and a temporary stabilization of the mechanical properties.
3. Prolonged hydrothermal exposure promoted further degradation of MOS hydration products, while carbonate-related diffraction features became more pronounced. As the residual MgO was gradually depleted, the formation of new hydration products became insufficient to compensate for the development of pores and microcracks. Consequently, pore coalescence, interfacial deterioration, and matrix damage became more pronounced, leading to further reductions in density and strength.

ACKNOWLEDGMENTS

The authors acknowledge the financial support provided by the Xuyun Technology Special Wood Industry Park Project in Huaxi District, Guiyang City: Design, Development, and Research of a Fully Automated Wood Panel Production Line (K22-0108-007).

Conflict of Interest

All authors declare that there are no conflicts of interest that could affect the publication of this manuscript. No commercial cooperation, patents, research funding, equity, labor remuneration or other potential interest associations exist.

Use of Generative AI

No generative artificial intelligence tools were used in the whole process of manuscript writing, data analysis and reference sorting. All images, figures, charts and schematics in this paper were independently drawn and photographed by the authors without AI generation.

REFERENCES CITED

Acda, M. N. (2022). "High-density fiberboard from wood and keratin fibers: Physical and mechanical properties," *Current Materials Science: Formerly: Recent Patents on Materials Science* 15(2), 154-163. https://doi.org/10.2174/2666145414666210906152353

Aiken, T. A., McPolin, D., Russell, M., Madden, M., and Bagnall, L. (2021). "Physical and mechanical performance of magnesium-based construction boards: A

comparative study," *Construction and Building Materials* 270, article 121397. https://doi.org/10.1016/j.conbuildmat.2020.121397

Azevedo, A. G. S., Baltazar, L., Faria, P., and Savastano, H. (2025). "Durability assessment of MgO-based fiber cement reinforced with lignocellulosic fibers and cured in a CO_2-rich atmosphere," *Journal of Building Engineering* 104, article 112327. https://doi.org/10.1016/j.conbuildmat.2024.136525

Azevedo, A. G. S., Filomeno, R., Gonçalves, M. M., Faria, P., and Savastano, H. (2024). "Innovative MOS-based fiber cement boards: Effect of kraft pulp mills waste and curing by accelerated carbonation," *Construction and Building Materials* 431, article 136525. https://doi.org/10.1016/J.JOBE.2025.112327

Bekhta, P., Sedliačik, J., Kačík, F., Noshchenko, G., and Kleinová, A. (2019). "Lignocellulosic waste fibers and their application as a component of urea-formaldehyde adhesive composition in the manufacture of plywood," *European Journal of Wood and Wood Products* 77(4), 495-508. https://doi.org/10.1007/s00107-019-01409-8

Calzaferri, G., Gallagher, S. H., Lustenberger, S., Walther, F., and Brühwiler, D. (2023). "Multiple equilibria description of type H1 hysteresis in gas sorption isotherms of mesoporous materials," *Materials Chemistry and Physics* 296, article 127121. https://doi.org/10.1016/j.matchemphys.2022.127121

Ding, L., Han, X., Chen, L., and Jiang, S. (2022). "Preparation and properties of hydrophobic and transparent wood," *Journal of Bioresources and Bioproducts* 7(4), 295-305. https://doi.org/10.1016/j.jobab.2022.02.001

Dong, T., Sheng, G., Zhang, A., Zhao, Z., Sun, X., Zhou, W., and Li, J. (2025). "Enhanced mechanical strength and water resistance of magnesium oxysulfate cement as wood adhesive," *International Journal of Adhesion and Adhesives* 142, article 104097. https://doi.org/10.1016/j.ijadhadh.2025.104097

GB/T 17657-2022 (2022). "Test methods for physical and chemical properties of wood-based panels and surface decorated wood-based panels," China Standards Press, Beijing, China.

Gu, K., Zhu, M., Song, Q., and Jiang, Z. (2024). "Hydration and microstructure formation of magnesium oxysulfate (MOS) cement regulated by sepiolite with high adsorption ability," *Cement and Concrete Composites* 153, article 105728. https://doi.org/10.1016/j.cemconcomp.2024.105728

Hou, Z., Li, J., Yang, H., and Cheng, Q. (2026). "Research on the modification of magnesium oxysulfate cement-based wood fiberboard by surfactants and organic phosphonic acids," *Case Studies in Construction Materials* 24, article e06016–e. https://doi.org/10.1016/j.cscm.2026.e06016

Ikubanni, P. P., Adeleke, A. A., Adekanye, T. A., Aladegboye, O. J., Agboola, O. O., and Ogunsemi, B. T. (2024). "Particleboard from biomass wastes: A review of production techniques, properties, and future trends," *Res. Eng. Struct. Mater* 10, 1-28. http://dx.doi.org/10.17515/resm2024.265ma0502rv

Li, Z.-G., Ji, Z.-S., Jiang, L.-L., and Yu, S.-W. (2017). "Effect of additives on the properties of magnesium oxysulfate cement," *Journal of Intelligent and Fuzzy Systems* 33(5), 3021-3025. https://doi.org/10.3233/JIFS-169353

Liu, Z., Han, C., Li, Q., Li, X., Zhou, H., Song, X., and Zu, F. (2022). "Study on wood chips modification and its application in wood-cement composites," *Case Studies in Construction Materials* 17, article e01350. https://doi.org/10.1016/j.cscm.2022.e01350

Luthfi, N., Wang, X., Kito, K., and Sunardi, S. (2020). "Effect of drying temperature on the mechanical properties of binderless fiberboard from bagasse: Study of flexural and tensile strength," *JIIF (Jurnal Ilmu dan Inovasi Fisika)* 4(2), 86-94. https://doi.org/10.24198/jiif.v4i2.28412

Neitzel, N., Hosseinpourpia, R., Walther, T., and Adamopoulos, S. (2022). "Alternative materials from agro-industry for wood panel manufacturing—A review," *Materials* 15(13), article 4542. https://doi.org/10.3390/ma15134542

Petrović, E. K., and Thomas, C. A. (2024). "Sustainability and toxicity of formaldehyde-based resins for composite wood products like plywood, particleboard and medium density fibreboard," *Sustainability and Toxicity of Building Materials* 2024, 389-415. https://doi.org/10.1016/B978-0-323-98336-5.00018-2

Przybek, A. (2025). "The role of natural fibers in the building industry—The perspective of sustainable development," *Materials* 18(16), article 3803. https://doi.org/10.3390/ma18163803

Sharma, S., Nandanwar, A., and Shukla, S. (2024). "Acoustical behavior of composite panel products produced from lignocellulosics," in: *Handbook of Vibroacoustics, Noise and Harshness*, Springer, pp. 659-691. https://doi.org/10.1007/978-981-97-8100-3_36

Sihag, K., Yadav, S. M., Lubis, M. A. R., Poonia, P. K., Negi, A., and Khali, D. P. (2022). "Influence of needle-punching treatment and pressure on selected properties of medium density fiberboard made of bamboo (*Dendrocalamus strictus* Roxb. Nees)," *Wood Material Science and Engineering* 17(6), 712-719. https://doi.org/10.1080/17480272.2021.1931440

Song, W., Zhu, M., and Zhang, S. (2018). "Comparison of the properties of fiberboard composites with bamboo green, wood, or their combination as the fibrous raw material," *BioResources* 13(2), 3315-3334. https://doi.org/10.15376/biores.13.2.3315-3334

Stark, N., and Cai, Z. (2021). "Wood-based composite materials: panel products, glued laminated timber, structural composite lumber, and wood–nonwood composites," Chapter 11 in: *FPL-GTR-282* 11–1–11–29. https://doi.org/10.1039/C2JM16699B

Theng, D., Arbat, G., Delgado-Aguilar, M., Ngo, B., Labonne, L., Mutjé, P., and Evon, P. (2019). "Production of fiberboard from rice straw thermomechanical extrudates by thermopressing: Influence of fiber morphology, water and lignin content," *European Journal of Wood and Wood Products* 77(1), 15-32. https://doi.org/10.1007/s00107-018-1358-0

Tupciauskas, R., and Rizhikovs, J. (2020). "Pre-treatment and investigation of wheat straw and hemp shives for binder-less fibreboard production," *AGROFOR Int. J.* 5, 80-87. https://doi.org/10.7251/AGRENG2003080T

Vitrone, F., Ramos, D., Ferrando, F., and Salvadó, J. (2021). "Binderless fiberboards for sustainable construction. Materials, production methods and applications," *Journal of Building Engineering* 44, article 102625. https://doi.org/10.1016/j.jobe.2021.102625

Wang, J., Cao, X., and Liu, H. (2021). "A review of the long-term effects of humidity on the mechanical properties of wood and wood-based products," *European Journal of Wood and Wood Products* 79(2), 245-259. https://doi.org/10.1007/s00107-020-01623-9

Xin, Z., Li, Y., Qiu, X., Zhang, H., Zhou, J., Yuan, J., Zong, Y., and Zhang, T. (2024). "Effects of environmental factors on natural aging of timber members of ancient buildings: Ultraviolet radiation, temperature and moisture," *Construction and*

Building Materials 456, article 139303. https://doi.org/10.1016/j.conbuildmat.2024.139303

Yan, J., Yang, C., Xue, B., Zhang, T., and Qu, W. (2024). "3D microstructural characterization and mechanical properties determination of poplar-ultrathin fiberboard," *Construction and Building Materials* 432, article 136662. https://doi.org/10.1016/j.conbuildmat.2024.136662

Yel, H. (2022). "Effect of alkaline pre-treatment and chemical additives on the performance of wood cement panels manufactured from sunflower stems," *Journal of Building Engineering* 52, article 104465. https://doi.org/10.1016/j.jobe.2022.104465

Zhang, J., Chen, N., Zhu, Z., Huang, Y., Chen, L., and Li, F. (2025). "Dual dynamic bonds synergy for reusable bio-based adhesive with superior mechanical robustness, environmental reliability, and mildew resistance," *NPG Asia Materials* 17(1), 31. https://doi.org/10.1038/s41427-025-00601-y

Zhang, J., Huang, Y., Aslani, F., Ma, G., and Nener, B. (2020). "A hybrid intelligent system for designing optimal proportions of recycled aggregate concrete," *Journal of Cleaner Production* 273, article 122922. https://doi.org/10.1016/j.jclepro.2020.122922

Zhang, T.-T., Zhang, J.-B., Chang, J., Bi, W.-L., Cheeseman, C., and Chen, X.-Y. (2024). "Hydration and strength development in magnesium oxysulfate (MOS) cement incorporating silicic acid," *Composites Part B* 268, article 111081. https://doi.org/10.1016/j.compositesb.2023.111081

Zhang, Z., Lin, B., Liu, T., and Liu, T. (2026). "Influence of $scCO_2$–H_2O Medium on the pore and fracture structure of coal at the time scale," *Natural Resources Research* 35, 1205–1227. https://doi.org/10.1007/s11053-025-10567-x

Article submitted: July 8, 2026; Peer review completed: August 8, 2026; Revised version received: August 18, 2026; Accepted: August 20, 2026; Published: September 10, 2026.
DOI: 10.15376/biores.21.4.10485-10503